Eur. Phys. J. Plus (2023) 138:1013
https://doi.org/10.1140/epjp/s13360-023-04630-w

THE EUROPEAN PHYSICAL JOURNAL PLUS

Regular Article

Influence of structural variables and external perturbations on the nonlinear optical rectification, second, and third-harmonic generation in the In*P*/InGaAs triple quantum well structure

M. Sayrac[1,a], **W. Belhadj**[2,b], **H. Dakhlaoui**[3,c], **F. Ungan**[4,d]

[1] Department of Nanotechnology Engineering, Sivas Cumhuriyet University, Sivas, Turkey
[2] Physics Department, Faculty of Applied Science, Umm AL-Qura University, Makkah, Saudi Arabia
[3] Physics Department, Nanomaterials Technology Unit, Basic and Applied Scientific Research Center (BASRC), College of Science of Dammam, Imam Abdulrahman Bin Faisal University, Dammam, Saudi Arabia
[4] Department of Physics, Sivas Cumhuriyet University, Sivas, Turkey

Received: 5 August 2023 / Accepted: 24 October 2023

Abstract The In*P*/InGaAs triple quantum well (TQW) structure is of significant interest to researchers studying new generations of semiconductor optoelectronic devices, as it offers valuable opportunities for controlling and enhancing the nonlinear optical processes in these devices. By applying external fields, such as hydrostatic pressure (P), temperature (T), and external electric field (F), the nonlinear optical properties of the In*P*/InGaAs TQW structure can be controlled and manipulated. This study investigates the effects of structure parameters of quantum well barriers and well widths (Lb and Lw) and the aforementioned external perturbations on the nonlinear optical properties, including the coefficients of nonlinear optical rectification (NOR), second-harmonic generation (SHG), and third-harmonic generation (THG) of the TQW structure. The energy eigenvalues and eigenfunctions of the confined single electron in TQW are obtained using the diagonalization method within the framework of the effective mass and parabolic band approximations. Moreover, employing the compact density matrix approximation for calculating the coefficients of the nonlinear optical response provides a computationally efficient way to assess the nonlinear optical properties of the TQW structure. The numerical results have significant potential to advance the understanding and design of semiconductor optoelectronic devices based on the In*P*/InGaAs triple quantum well structure. Exploring the effects of different parameters and external fields can lead to deeper insights into the underlying physics and may unlock new opportunities for developing innovative and high-performance devices.

1 Introduction

In recent decades, nonlinear optics has indeed been an active and rapidly developing field of research, which has some key areas of progress for nonlinear optical materials [1–9]. Nonlinear optical materials exhibit a range of interesting phenomena, such as frequency conversion, optical parametric amplification, and generation of ultrashort laser pulses. These materials are used in various applications, including optical modulators [10], laser technology [11], and detectors [12], to name just a few. The development of nonlinear optical materials has been driven by advances in material science, nanotechnology, and fabrication techniques. Researchers have focused on designing and synthesizing materials with enhanced nonlinear optical properties, such as high nonlinear coefficients and low optical losses. Furthermore, the field of nonlinear optics has benefited from the development of ultrafast laser technology. These intense and ultrashort laser pulses provide a unique tool for studying nonlinear optical processes and characterizing the response of materials at extremely high temporal resolutions. In addition to the development of the above-mentioned areas, the diversification of low-dimensional semiconductor nanostructures, including quantum dots (QDs), quantum wires, and quantum wells, has indeed sparked extensive research in the fields of condensed matter physics and optoelectronics. These structures offer unique electrical and optical properties that have attracted significant attention and led to important advancements. In recent years, there has been a surge of theoretical studies focused on investigating the second-order nonlinear optical properties, such as NOR, SHG, and THG, of various semiconductor materials and different geometries of quantum wells [13–17]. The investigation of the linear and nonlinear optical properties of InAs/GaAs structures is explored by Makhlouf et al. [18]. Zeiri et al. [19] investigated the absorption coefficients (ACs), and relative refractive index changes (RRIC) in quantum wells by using the density matrix approach.

[a] e-mail: muhammedsayrac@cumhuriyet.edu.tr (corresponding author)
[b] e-mail: wbbelhadj@uqu.edu.sa
[c] e-mail: hbaldkhlaen@iau.edu.sa
[d] e-mail: fungan@cumhuriyet.edu.tr

Published online: 14 November 2023

Dahiya et al. explored the effects of temperature and hydrostatic pressure on the optical properties of semi-parabolic QD [20]. The effect of intense laser fields (ILF) on the optical properties of graded QWs was investigated by Kasapoglu [21]. Mahrsia et al. investigated the thermodynamic effects on the nonlinear optical response of vertically coupled lens-shaped InAs/GaAs quantum dots [22]. Chen et al. explored absorption coefficients in a double triangular quantum well exposed to external electric fields [23]. The effects of ILF on NOR, SHG, and THG of the squared quantum well were investigated [24].

In this paper, the nonlinear optical properties (NOR, SHG, and THG) of In*P*/InGaAs TQW structure at different structure parameters and external perturbation are investigated in detail. The In*P*/InGaAs TQW structure is significant in semiconductor optoelectronic devices because it enables precise control over the optical and electronic properties of the material, leading to improved performance, wavelength tunability, and versatility in a wide range of applications, particularly in the fields of telecommunications and photonics. The novelty of the paper is to computationally consider the nonlinear optical properties of the In*P*/InGaAs structure under the influence of structure parameters and applied external probes, which results in significant changes in the investigated optical responses. These external factors like hydrostatic pressure (P), temperature (T), and external electric field (F) can indeed be used to control and enhance the nonlinear optical properties of the In*P*/InGaAs TQW structure. These factors can modify the material's electronic band structure and carrier dynamics, which, in turn, affect nonlinear optical properties employing controlling the change in the lattice constants, shifting the bandgap energy and modification of the energy levels in the quantum wells. Experimental investigations of nonlinear optical properties can be time-consuming, expensive, and technically challenging. The computational simulations enable the modeling, prediction, and analysis of the nonlinear optical properties of semiconductor structures and offer a more efficient and cost-effective alternative by rapidly exploring a large parameter space and providing valuable insights into the system behavior. The paper employs effective mass and parabolic band approximations to model the system. By employing these approximations, the paper aims to study the impact of structure parameters and external probes on the nonlinear optical properties of the In*P*/InGaAs structure. The approach involves main two steps to investigate the nonlinear optical properties of In*P*/InGaAs quantum wells. The first step is to calculate the eigenvalues and eigenfunctions of the In*P*/InGaAs quantum well structure by solving the Schrödinger wave equation using the effective mass approximation. The second step is that the compact density matrix approach and the iterative method are utilized to determine the optical coefficients associated with the nonlinear optical properties of the In*P*/InGaAs quantum well. A breakdown of the different sections of the paper consists of Sect. 1: Introduction, Sect. 2: Theoretical Description, Sect. 3: Simulation Results, and finally Sect. 4: Conclusion.

2 Theory

This study investigates the $In_xGa_{1-x}As/InP$ TQW, which is a semiconductor device that exhibits unique optical properties due to the quantum confinement of electrons in the InGaAs layers. The mentioned study aims to investigate the nonlinear optical properties of the TQW structure exposed to structural parameters and external probes. We explored how the structural parameters of the TQW and the impact of external probes, such as the barrier thickness, well width, hydrostatic pressure, temperature, and external electric field influence the nonlinear optical properties. By varying these parameters, they can tune the energy levels of the confined electrons and modify the optical response of the TQW structure. The schematic presentation of the TQW structure is given in Fig. 1.

This structure consists of the InGaAs structure, which is sandwiched between In*P* layers. The configuration of the structure stetting: $z_1 = 3$ nm, z_2–$z_1 = \mathrm{Lw}_L$, z_3–$z_2 = \mathrm{Lb}_L$, z_4–$z_3 = \mathrm{Lw}_C$, z_5–$z_4 = \mathrm{Lb}_R$, z_6–$z_5 = \mathrm{Lw}_R$, z_7–$z_6 = 3$ nm, $V_0 = 518$ meV (quantum well depth for the composition of $x = 0.53$). Lw_L, Lw_C, Lw_R, Lb_L, and Lb_R are left well width, center well width, right well width, left barrier thickness, and right barrier thickness, respectively.

The total Hamiltonian of an electron confined in InGaAs /In*P* structure in the presence of the applied external z-oriented electric field within the framework of effective mass and parabolic band approximations is given by [25–27]

$$H = \frac{\vec{p}_e^2}{2m^*(P,T)} + V(z,P,T) - eF\vec{z} \tag{1}$$

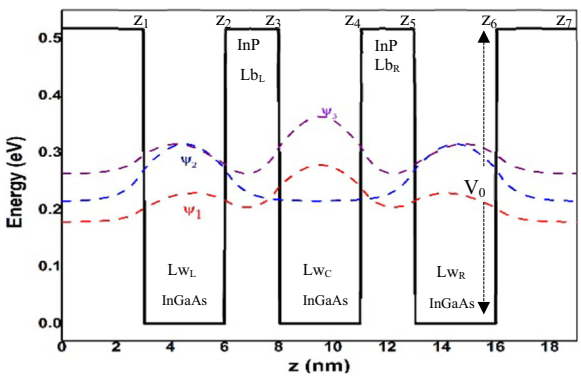

Fig. 1 TQW of InGaAs/In*P* structure and the corresponding wave functions. Lw_L: left well width, Lw_C: center well width, Lw_R: right well width, Lb_L: left barrier thickness, Lb_R: right barrier thickness, V_0: quantum well depth

where $m^*(P, T)$ is the electron effective mass, P_e is the electron momentum, F is the magnitude of the applied external electric field, and the z-axis is the growth direction of the structure. The Hamiltonian in Eq. 1 can be used to solve the Schrödinger equation and obtain the energy levels and wave functions, which, in turn, affect the optical properties of the material. The hydrostatic pressure (P) and temperature (T) dependency of electron effective mass are given by

$$m^*(P,T) = \left[1 + E_P^{\Gamma}\left(\frac{2}{E_g^{\Gamma}(P,T)} + \frac{1}{E_g^{\Gamma}(P,T) + 0.341}\right)\right]^{-1} m_0 \tag{2}$$

where m_0 is the free electron mass [28].

In addition, $E_g^{\Gamma}(P,\ T)$, the energy gap (eV) for InP, depends on pressure and temperature.

$$E_g^{\Gamma}(P,T) = E_g^0(0,T) + \alpha P - \beta P^2\ (\text{eV}) \tag{3}$$

where $\alpha = 8.4 \times 10^{-3}$ and $\beta = 1.8 \times 10^{-5}$ are the pressure coefficients for InP [29]. $E_g^{\Gamma}(0,\ T)$ is the temperature-dependent energy gap and given as

$$E_g^{\Gamma}(0,T) = 1.421 + \eta T^2 (T + c)^{-1}\ (\text{eV}) \tag{4}$$

where $\eta = 4.9 \times 10^{-4}$ and $c = 327K$ are the temperature coefficients for InP [29]. Energy band gap for InGaAs is $E_g\ (x,T) = 0.42 + 0.625x - [5.8/(T + 300) - 4.19/(T + 271)]\cdot 10^{-4} T^2 x - 4.19\cdot 10^{-4} T^2/(T + 271) + 0.475x^2$ (eV). The pressure dependence of the energy band gap for InGaAs is $E_g\ (0.47, P) \sim = (0.733 + 11.0 \times 10^{-3} P - 27 \times 10^{-6}\ P^2)$ eV [30].

The pressure coefficient indicates the change in bandgap energy per unit pressure. In the case of InP, for every increase in pressure of 1 GPa, the bandgap energy of InP will vary by approximately 0.07 eV. The temperature coefficient, similarly, represents the change in bandgap energy per unit temperature. For InP, for every increase in temperature of 1 Kelvin ($^{\circ}K$), the bandgap energy will change by approximately 0.5 meV [28].

The confining potential also is affected by the temperature and the pressure and is given by

$$V(z,P,T) = G_{c(v)}\left(E_g^{\text{In}P}(P,T) - E_g^{\text{InGaAs}}(P,T)\right) \tag{5}$$

where the conductance and valance band offset parameters ($G_{c(v)}$) are assumed to remain constant with pressure for InP/InGaAs. The ratio is taken as 0.38:0.62 [31, 32].

The confinement potential ($V(z,\ P,\ T)$) for an electron in the z-direction within a material depends on the specific structure, and properties of the material is described as:

$$V(z,P,T) = \begin{cases} V_0(z,P,T) & 0 < z < z_1 \\ 0 & z_1 < z < z_2 \\ V_0(z,P,T) & z_2 < z < z_3 \\ 0 & z_3 < z < z_4 \\ V_0(z,P,T) & z_4 < z < z_5 \\ 0 & z_5 < z < z_6 \\ V_0(z,P,T) & z_6 < z < z_7 \end{cases} \tag{6}$$

The TQW width as a function of hydrostatic pressure depends on the material's response to changes in lattice constant. The TQW width can be affected by hydrostatic pressure-induced changes in the lattice constant, which can alter the bandgap energy and affect the width of the QW. The QW width as a function of the hydrostatic pressure is given as [33]

$$L(P) = L(0)(1 - (S_{11} + 2S_{12})P) \tag{7}$$

Here, $L(0)$ is the QW width without hydrostatic pressure, and S_{11} and S_{22} elastic constants for InGaAs are given below [32].

$$\begin{aligned} S_{11} &= \frac{C_{11} + C_{12}}{(C_{11} - C_{12}) * (C_{11} + 2C_{12})}; \quad S_{12} = \frac{-C_{12}}{(C_{11} - C_{12}) * (C_{11} + 2C_{12})} \\ C_{11} &= (8.34 + 3.56 * x) * 10; \quad C_{12} = (4.54 + 0.80 * x) * 10 \end{aligned} \tag{8}$$

The subband energy levels and wave functions of electrons in a quantum well structure can be obtained by solving the time-independent Schrödinger equation. The wave function describes the spatial distribution and behavior of the electron within the quantum well.

In the case of a quantum well, the wave function is typically described as a standing wave. Within the quantum well region, the wave function exhibits oscillatory behavior and is generally characterized by a combination of sine and cosine functions. The number of oscillations depends on the energy level of the electron and the width of the quantum well.

In the barrier regions surrounding the well, the wave function decays exponentially as the electron moves away from the well. The amplitude of the wave function decreases rapidly within the barriers, indicating that the probability of finding the electron outside the well is very low. The exact form of the wave functions is influenced by various factors such as the thicknesses and compositions

of the layers, as well as the specific energy level of the electrons. The wave functions are eigenfunctions of the Schrödinger equation, corresponding to the allowed energy levels or subbands of the quantum well structure.

The variation of the structure parameters and external probes can be accounted for by adjusting the potential energy profile in the Hamiltonian matrix to study their effects on the subband energy levels and wave functions. The diagonalization method is a common approach used to calculate the subband energy levels and corresponding wave functions in quantum well structures [34]. In this method, the calculation of the single-electron wave function $\psi(z)$ is performed for infinite quantum well width L_∞, which is large compared to the TQW widths. The wave function describing the structure is given as:

$$\psi(z) = \sqrt{\frac{2}{L_\infty}} \sum_{m=1}^{\infty} C_m \sin\left(m\pi\left[\frac{z}{L_\infty} + \frac{1}{2}\right]\right) \tag{9}$$

After defining the hydrostatic pressure- and temperature-dependent structural parameters, the energies and corresponding wave functions can be obtained by solving the Schrödinger equation that incorporates these effects. Then, the nonlinear optical coefficients of NOR, SHG, and THG in the TQW are calculated by considering the compact density matrix approach and an iterative procedure [35–38].

The NOR, SHG, and THG coefficients are defined as [39]:

$$\chi_0^{(2)} = \frac{4e^3\rho_{01}}{\varepsilon_0\hbar^2} \frac{\mu_{01}^2\delta_{01}\left[\omega_{10}^2\left(1 + \Gamma_2/\Gamma_1\right) + \left(\omega^2 + \Gamma_2^2\right)\left(\Gamma_2/\Gamma_1 - 1\right)\right]}{\left[(\omega_{10} - \omega)^2 + \Gamma_2^2\right]\left[(\omega_{10} + \omega)^2 + \Gamma_2^2\right]} \tag{10}$$

$$\chi_{2\omega}^{(2)} = \frac{e^3\rho_{01}}{\varepsilon_0\hbar^2} \frac{\mu_{01}\mu_{12}\mu_{20}}{(\omega - \omega_{10} - i\Gamma_3)(2\omega - \omega_{20} - i\Gamma_3)} \tag{11}$$

$$\chi_{3\omega}^{(3)} = \frac{e^4\rho_{03}}{\varepsilon_0\hbar^3} \frac{\mu_{01}\mu_{12}\mu_{23}\mu_{30}}{(\omega - \omega_{10} - i\Gamma_3)(2\omega - \omega_{20} - i\Gamma_3)(3\omega - \omega_{30} - i\Gamma_3)} \tag{12}$$

where $\rho_{0i} = \rho_0 - \rho_i$, $i = 1, 3$ term is the three-dimensional concentration (number density) of electrons involved in the transition. $\mu_{ij} = \langle\psi_i|z|\,\psi_j\rangle$, $(i,\ j = 0,\ 1,\ 2,\ 3)$ is the off-diagonal matrix element. It characterizes the strength of the interaction between the two levels involved in the transition. δ_{10} is $\delta_{10} = |\mu_{00} - \mu_{11}|$, $\omega_{ij} = \left(E_i - E_j\right)/\hbar$ is the transition frequency, and $\Gamma_k = 1/T_k$, $(k = 1, 2, 3)$ is the coefficient that indicates the relaxation rate related to the transition lifetime of the electrons.

3 Results and discussion

In this section, the effects of structure parameters and external probes on the NOR, SHG, and THG coefficients in the TQW structure are discussed. To perform the calculation of the nonlinear optical coefficients, various simulation input parameters need to be considered. $m^* = 0.077m_0$ (where m_0 is the free electron mass), $e = 1.602 \times 10^{-19}$ C, $\hbar = 1.056 \times 10^{-34}$ Js, $\rho_{01} = \rho_{03} = 3 \times 10^{22}$ m^{-3}, $\mu = 4\pi \times 10^7$ Hm^{-1}, $\varepsilon = 13.9$, $\varepsilon_0 = 8.854 \times 10^{-12}$, and $\Gamma_k (k = 1, 2, 3)$ is 1, 5, and 7 THz, respectively. To obtain the optical coefficients, initially, the subband energy levels and their envelope wave functions are obtained by using the effective mass and the single parabolic band approximations. Then, the nonlinear optical properties of the structure are calculated by using the compact density matrix approximation.

Tables give information about the energy differences (in meV) and dipole moment matrix elements (in angstrom) at different structure parameters and external probes.

In Fig. 2a, the left–right barrier thickness ($\mathrm{Lb}_L = \mathrm{Lb}_R$) ranges from 2 to 5nm, and it shows the variation of NOR coefficients at different barrier thicknesses. According to Table 1, as the barrier thickness increases, the ground and first excited state energy differences (E_{10}) decrease. This decrease in energy difference leads to a redshift of the NOR coefficients. Additionally, Table 1 indicates that the dipole matrix elements (${\mu_{01}}^2\delta_{01}$) increase as the barrier thickness increases. The dipole matrix elements directly influence the amplitude of the NOR coefficients. Therefore, with the increasing barrier thickness, the amplitude of the NOR coefficient increases. The increase in the dipole matrix elements is due to the enhancement of the overlap between the ground and first excited wave functions. In fact, by increasing the widths of the internal barriers $\mathrm{Lb_L}$ and $\mathrm{Lb_R}$, the two wave functions are reinforced in the QW regions, and their separation in the barriers is strongly limited. This leads to an increase in the dipole matrix elements and in turn an augmentation of the NOR amplitudes.

Figure 2b shows the variation of NOR coefficients at different quantum well widths ($\mathrm{Lw}_L = \mathrm{Lw}_C = \mathrm{Lw}_R$). The NOR coefficients are redshifted with the increment in the quantum well widths (Table 2). This is because the ground and first excited state energy differences (E_{10}) decrease as the well width increases. Table 2 also indicates that the dipole matrix elements increase with the increment in the quantum well width. This increase in dipole matrix elements leads to an increase in the amplitude of the NOR coefficients. Therefore, the amplitude of the NOR resonant peaks is expected to increase with the widening of the quantum well. The amplitude of the NOR resonant peaks is related to the variation of transition dipole moment (${\mu_{01}}^2\delta_{01}$) as a function of the structural parameters. As the quantum well width changes, it affects the transition dipole moment, resulting in the observed changes in the

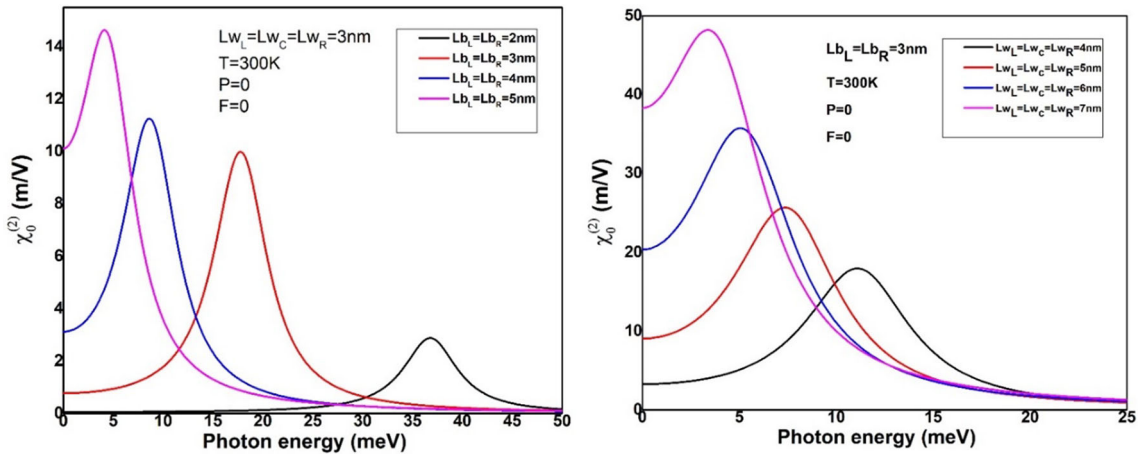

Fig. 2 Variation of NOR for different barrier thicknesses (Lb) and quantum well width (Lw)

Table 1 Effects of the left and right barrier thicknesses (Lb = $Lb_L = Lb_R$)

Lb	E_{10}	E_{20}	E_{30}	${\mu_{01}}^2\delta_{01}$	$\mu_{01}\mu_{12}\mu_{20}$	$\mu_{01}\mu_{12}\mu_{23}\mu_{30}$
2	36.81	84.61	543.77	12.52	4.68	2.47
3	17.81	37.77	480.24	14.27	17.03	4.26
4	8.75	17.19	434.37	15.82	32.42	5.94
5	4.44	7.93	402.51	17.25	35.11	7.25

Table 2 Effects of the left, center, and right quantum well widths ($Lw = Lw_L = Lw_C = Lw_R$)

Lw	E_{10}	E_{20}	E_{30}	${\mu_{01}}^2\delta_{01}$	$\mu_{01}\mu_{12}\mu_{20}$	$\mu_{01}\mu_{12}\mu_{23}\mu_{30}$
4	11.19	23.22	408.63	23.73	81.88	0.96
5	7.51	15.39	338.90	30.98	119.02	1.66
6	5.30	10.77	280.02	39.20	166.87	2.61
7	3.79	7.85	233.01	47.01	208.98	3.82

amplitude of the NOR resonant peaks. Furthermore, by comparing Fig. 2a, b, we observe that the increase in the NOR amplitude is more perceptible by increasing well widths than barrier widths. This result is a consequence of the strong values of the dipole matrix elements in the case of enlarging well widths. Every increase in the QW widths introduces an additional spread of each wave function and results in a strong augmentation in the dipole matrix elements of the ground and first excited waves.

Figure 3a illustrates the effect of hydrostatic pressure on the properties of a system, particularly on the effective mass and dielectric constant, and how these pressure changes result in a redshift in the NOR resonant peak positions. The variation of NOR coefficients shows a redshift as the pressure changes. This can be attributed to the decrease in the ground and first excited state energy differences (E_{10}) with varied pressure, as seen in Table 3. Table 3 also indicates that the dipole matrix elements have a small change with the increment in the applied pressure. This suggests that the applied pressure has a minimal effect on the dipole matrix elements. As a result, the amplitude of the NOR coefficients exhibits a small variation. Considering the negligible change in the dipole matrix elements (${\mu_{01}}^2\delta_{01}$), the overall effect of increasing pressure on the dipole matrix elements appears to be insignificant. From a mathematical point of view, this weak influence of the hydrostatic pressure is explained by examining the analytical expressions ((Eq. 3) and (Eq. 7)). In these expressions, the hydrostatic pressure P is multiplied by smaller factors. For instance, the expression of the energy gap (expression 3) contains the term βP^2. In that term, β is equal to 1.810^{-5}. This makes the small values of hydrostatic pressure not largely sensitive, and consequently, the amplitudes of (NOR) present a limited variation by varying the hydrostatic pressure. Figure 3b represents the changes in temperature causing the NOR coefficient peak position to shift to higher energies. The variation of NOR coefficients shows a blueshift as the temperature increases. This is because the ground and first excited state energy differences (E_{10}) increase with the applied temperature, as indicated in Table 4. Table 4 also confirms that the dipole matrix elements increase (${\mu_{01}}^2\delta_{01}$) with the increment in the temperature. The increased temperature causes an increase in the average kinetic energy of the particles within the system, leading to enhanced electronic transitions. These enhanced transitions influence the dipole matrix elements, resulting in the resonant NOR peak increase.

Overall, the effects of the hydrostatic pressure and temperature could be discussed in detail below. When hydrostatic pressure is applied to a material or system, it can cause changes in the crystal lattice or the electronic structure. These changes affect the properties of the charge carriers within the material, leading to modifications in the effective mass and dielectric constant. As the hydrostatic pressure increases, the effective mass of charge carriers decreases. This decrease in effective mass implies that the charge

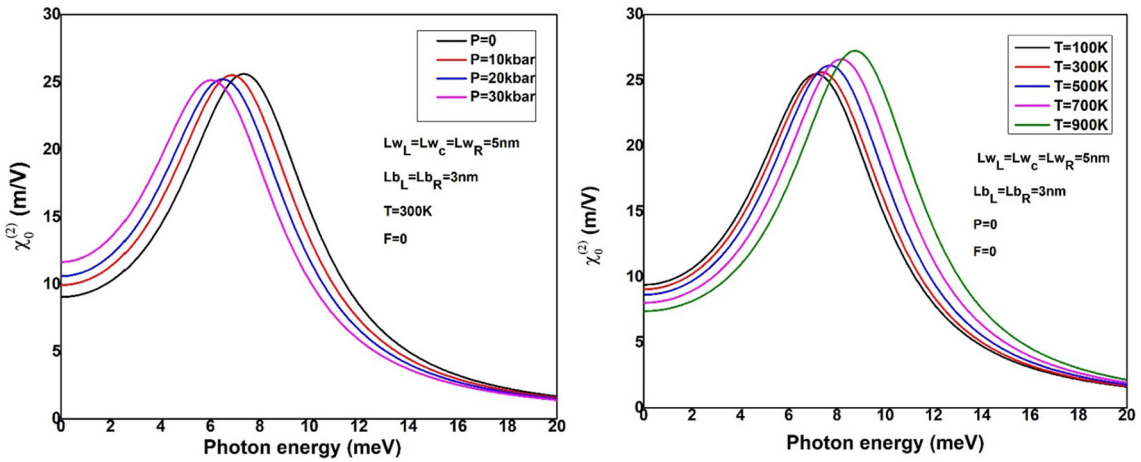

Fig. 3 Variations of NOR for different pressure (P) and temperature (T)

Table 3 Effects of the hydrostatic pressure (kbar)

P	E_{10}	E_{20}	E_{30}	$\mu_{01}{}^2\delta_{01}$	$\mu_{01}\mu_{12}\mu_{20}$	$\mu_{01}\mu_{12}\mu_{23}\mu_{30}$
0	7.51	15.39	338.90	30.98	119.02	1.30
10	7.04	14.82	334.85	31.00	118.14	1.35
20	6.68	14.28	330.94	31.01	117.67	1.36
30	6.23	13.76	327.17	31.02	117.55	1.38

Table 4 Effects of the temperatures (K)

T	E_{10}	E_{20}	E_{30}	$\mu_{01}{}^2\delta_{01}$	$\mu_{01}\mu_{12}\mu_{20}$	$\mu_{01}\mu_{12}\mu_{23}\mu_{30}$
100	7.30	15.15	340.92	30.00	115.95	1.30
300	7.51	15.39	338.90	30.98	119.02	1.31
500	7.85	16.09	332.94	31.15	128.56	1.32
700	8.31	17.09	324.90	31.65	142.45	1.35
900	8.88	18.30	315.63	31.86	160.11	1.37

carriers become more mobile, responding more easily to external forces. Simultaneously, the dielectric constant of the material also decreases under higher hydrostatic pressure. This decrease in dielectric constant suggests that the material becomes less polarizable and less responsive to electric fields. The reduction in effective mass and dielectric constant contributes to a decrease in energy differences within the material. Therefore, the redshift is observed in NOR resonant peak positions. On the other hand, when the temperature of a material increases, the effective mass of charge carriers also increases due to the enhanced interaction with lattice vibrations. This results in charge carriers being less mobile and less responsive to external forces. Additionally, the dielectric constant of the material decreases as thermal energy disrupts the alignment of atoms. These changes in effective mass and dielectric constant lead to an increase in energy differences within the material. For this reason, the NOR peak position blueshifts. Similarly, both SHG and THG coefficients are also affected by the hydrostatic pressure and temperature.

Figure 4 presents the change of NOR coefficients associated with the optical response of TQW as a function of the applied external electric fields. The effect of an electric field on the NOR coefficients and dipole moment matrix element can be significant. When an electric field is applied, it can induce changes in the energy levels and wave functions of the system, leading to alterations in the NOR coefficients and dipole moment matrix elements. The electric field can shift the energy levels of the system, including the ground and excited states. This shift can result in changes in the energy differences between these states, affecting the NOR coefficient. In Fig. 4, the NOR coefficient's peak positions exhibit a blueshift caused by the increase in the energy difference between the ground states and the first excited states (Table 5). Furthermore, the electric field can modify the wave functions of the system, which directly impacts the dipole moment matrix elements. As the electric field increases, the dipole moment matrix elements experience a decrease because of the decrement in the square of the dipole matrix element ($\mu_{01}{}^2\delta_{01}$ seen in Table 5). Due to the electrostatic interaction introduced by the electric field, the electrons are pushed in the opposite direction of the electric field. In addition to the orthogonality condition between the wave functions, the overlap between the ground and first excited wave function is reduced leading to a decrease in the dipole matrix elements as justified by Table 5. As a consequence, the amplitudes of the (NOR) are considerably diminished.

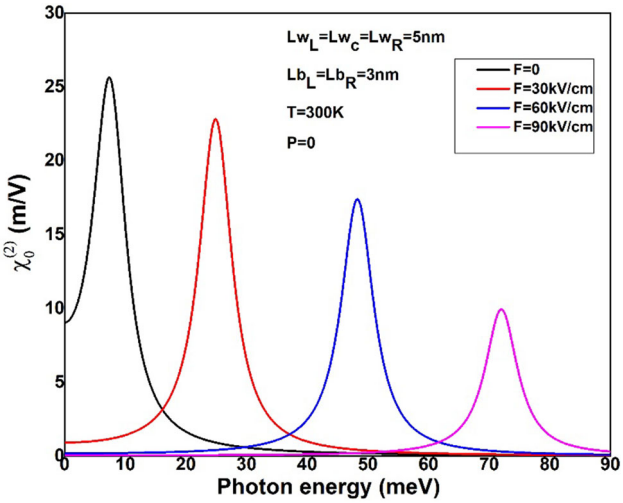

Fig. 4 Variations of NOR for the different applied electric fields (F)

Table 5 Effects of the applied electric field (kV/cm)

F	E_{10}	E_{20}	E_{30}	$\mu_{01}{}^2\delta_{01}$	$\mu_{01}\mu_{12}\mu_{20}$	$\mu_{01}\mu_{12}\mu_{23}\mu_{30}$
0	7.51	15.39	338.90	30.98	119.02	1.80
30	24.93	50.35	349.83	8.57	63.10	1.48
60	48.28	97.08	357.87	4.07	53.66	0.51
90	72.02	144.58	362.39	3.07	39.29	0.25

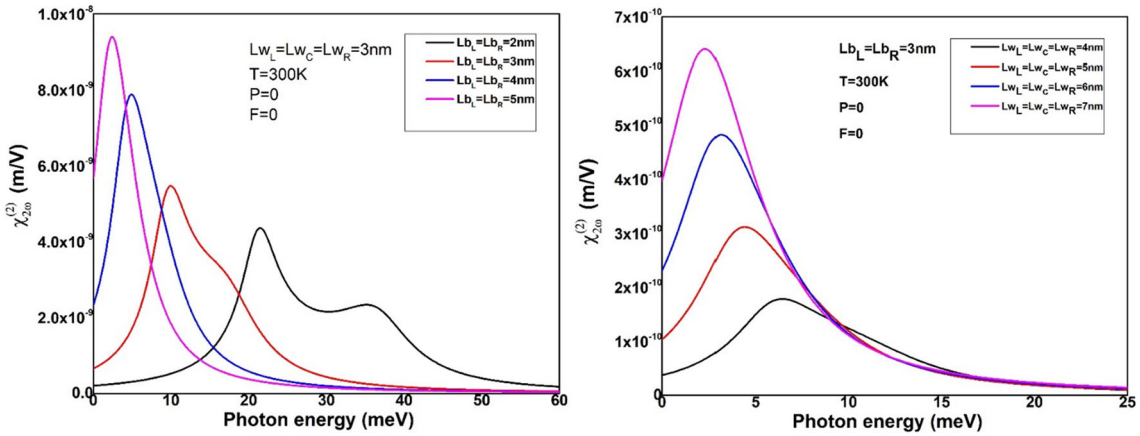

Fig. 5 Variations of SHG for different barrier thicknesses (Lb) and barrier width (Lw)

In general, the presence of an electric field can influence both the NOR coefficients and dipole moment matrix elements. It can alter the energy differences between states, leading to shifts in the NOR coefficients, and modify the transition probabilities, affecting the dipole moment matrix elements.

In Fig. 5, the variation of second-harmonic generation (SHG) coefficients is observed as the quantum barrier thickness (Lb) and quantum well widths (Lw) increase. According to Fig. 5a, the SHG coefficients display a redshift as the barrier thickness increases. This redshift can be attributed to the decrease in the energy difference (E_{20}) between the ground state and the second excited state with increasing Lb. Additionally, Table 1 suggests that the product of the dipole matrix elements ($\mu_{01}\mu_{12}\mu_{20}$) increases with the increment in Lb. This indicates that the dipole matrix elements associated with the electronic transitions involved in SHG also increase as the barrier thickness increases. The noticeable effect of barrier thickness on the SHG coefficients further supports the influence of Lb on the electronic transitions and the dipole matrix elements. These findings suggest that adjusting the barrier thickness can impact the efficiency and optical properties of the second-harmonic generation.

Figure 5b shows the variation of SHG coefficients as the quantum well width (Lw) changes. The SHG coefficient experiences redshifts. This shift can be attributed to the increase in the energy difference (E_{20}) between the ground state and the second excited state as the well width increases. Table 2 indicates that the $\mu_{01}\mu_{12}\mu_{20}$ product increases with the increment in Lw. This implies that the dipole matrix elements associated with the electronic transitions relevant to SHG also increase as the well width increases.

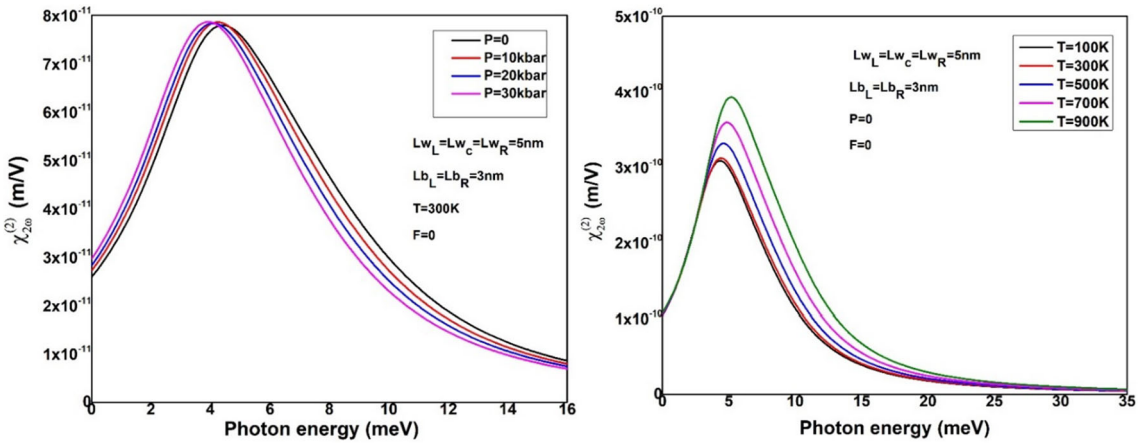

Fig. 6 Variations of SHG for different pressure (P) and temperature (T)

Quantum barrier widths refer to the width of potential energy barriers within a system. These barriers can influence particle behavior, such as their ability to move or interact with each other. In the context of electronic transitions and dipole matrix elements, wider barriers can affect wave function overlap and the spatial extent of electronic states involved in the transition, thereby modifying the dipole matrix elements associated with these transitions. These findings suggest that both quantum barrier widths (Lb) and quantum well widths (Lw) play important roles in determining the SHG coefficients and dipole matrix elements. Adjusting these widths can have significant effects on the electronic transitions and optical properties in the studied system.

In Fig. 6a the SHG coefficients show a slight redshift as the applied hydrostatic pressure increases. This redshift can be attributed to the decrease in the energy difference (E_{20}) between the ground and the second excited states as the pressure increases, as indicated in Table 3. Table 3 also suggests that the product of the dipole matrix elements ($\mu_{01}\mu_{12}\mu_{20}$) slightly varies with the increment in the applied pressure. However, the variation appears to be minimal, indicating that the applied pressure has a negligible effect on the dipole matrix elements. Considering the small change in the dipole matrix elements, the overall effect of increasing pressure on the dipole matrix elements seems to be insignificant. As a result, the amplitude of the SHG coefficients exhibits only a small variation with increasing pressure.

In Fig. 6b, the SHG coefficients exhibit a blue shift as the applied temperature increases. This blue shift can be attributed to the increase in the energy difference of E_{20}, as seen in Table 4. Table 4 also confirms that the product of the dipole matrix elements increases with the increment in the temperature. The increased temperature leads to an increase in the average kinetic energy of the particles within the system, which, in turn, enhances electronic transitions. These enhanced transitions influence the dipole matrix elements and result in their increase. The increased dipole matrix elements directly affect the amplitude of the SHG coefficients. Consequently, the amplitude of the SHG resonant peaks is expected to change as the temperature varies, exhibiting a small blueshift due to the increased ground and first excited state energy differences. The relationship between temperature, electronic transitions, and dipole matrix elements is consistent with the behavior observed in the system being studied.

The application of an external electric field has a significant effect on the SHG coefficients and dipole moment matrix elements in the studied system. When an electric field is applied, it induces changes in the energy levels and wave functions of the system, resulting in alterations in the SHG coefficients and dipole moment matrix elements. The electric field can shift the energy levels of the system, including the ground and excited states. This shift in energy levels influences the energy differences between these states, which affects the SHG coefficients.

In Fig. 7, the peak positions of the SHG coefficients exhibit a blueshift, which can be attributed to the increased energy difference between the ground and second excited states (E_{02}), as indicated in Table 5. Additionally, the electric field can modify the wave functions of the system, directly impacting the dipole moment matrix elements. As the electric field increases, the product of the dipole moment matrix elements experiences a decrease due to the decrease in the product of the dipole moment matrix elements ($\mu_{10}\mu_{12}\mu_{20}$, as mentioned in Table 5). The presence of an electric field has a notable influence on both the SHG coefficients and dipole moment matrix elements. It can alter the energy differences between states, leading to shifts in the SHG coefficients, and modify the transition probabilities, affecting the dipole moment matrix elements.

Figure 8 illustrates the changes in the third-harmonic generation (THG) coefficients at different structure parameters, specifically focusing on the barrier thickness (Lb) and the quantum well widths (Lw). In Fig. 8a, the effects of the barrier thickness ($\mathrm{Lb}_L = \mathrm{Lb}_R = 2, 3, 4, 5$ nm) are investigated, resulting in the resonant peak of the THG redshifts. The redshift occurs because the energy difference (E_{30}) between the ground state and the third excited state decreases with an increase in Lb, as indicated in Table 1. This suggests that the energy levels of the system become closer together, which leads to a lower energy gap for the THG process to occur. In addition, Table 1 provides information on the product of the dipole matrix elements ($\mu_{01}\mu_{12}\mu_{23}\mu_{30}$), which are observed to increase with the increment in the barrier thickness ($\mathrm{L_b}$). This increase in the dipole matrix elements directly affects the amplitude

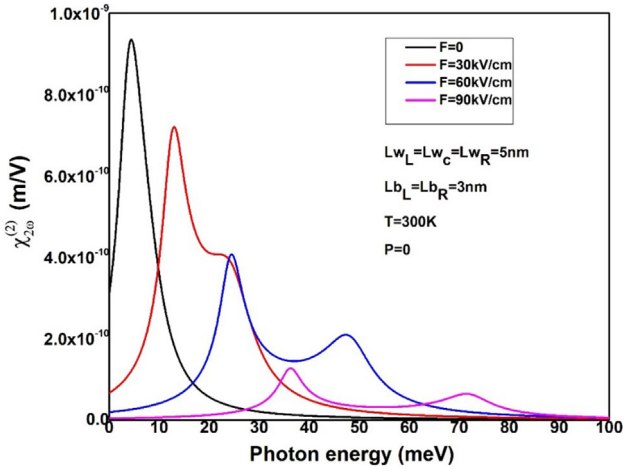

Fig. 7 Variations of SHG for the different applied electric fields (F)

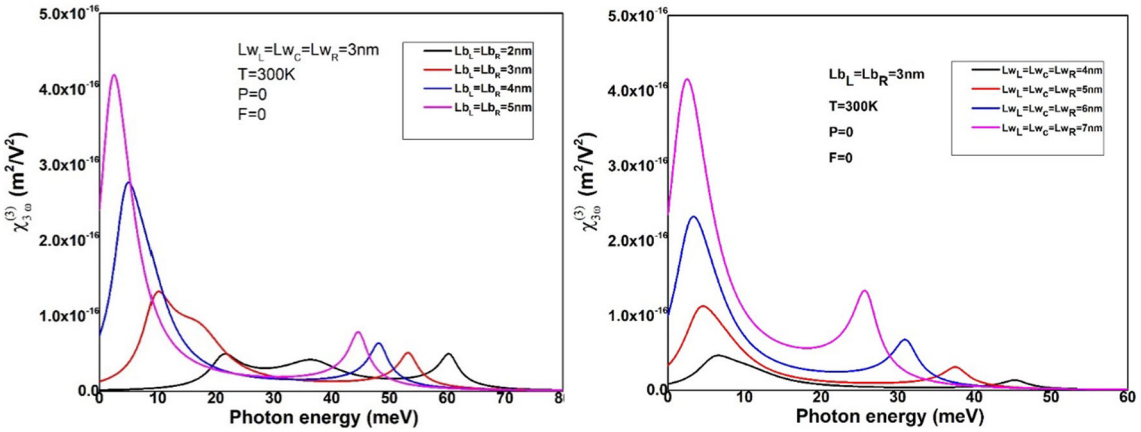

Fig. 8 Variations of THG for different barrier thicknesses (Lb) and barrier width (Lw)

of the THG coefficients. The product dipole matrix elements quantify the strength of the dipole–dipole interaction between the involved states (e.g., ground state and excited states). As the barrier thickness increases, the strength of the dipole–dipole interaction between the quantum states or energy levels within the material becomes stronger. This indicates a higher likelihood of efficient energy transfer and interaction between the states, which contributes to a larger amplitude of the THG coefficients. In Fig. 8b, the third-harmonic generation (THG) coefficients at different quantum well widths (Lw) are presented. The observations in this figure indicate a redshift of the THG resonant peaks and an increase in the THG peak amplitude. The redshift of the resonant peaks in the THG response is caused by the decrement in the energy difference (E_{30}) between the ground state and the third excited state as the quantum well width (Lw) increases. This decreasing energy difference implies that the energy levels of the system become closer together, leading to a lower energy gap for the THG process to occur. Consequently, the resonant peak of the THG response shifts toward longer wavelengths, resulting in the observed redshift. Furthermore, as the quantum well width (Lw) increases, the product dipole matrix elements increase ($\mu_{01}\mu_{12}\mu_{23}\mu_{30}$), which enhances the dipole–dipole interaction between the relevant states. This strengthened interaction facilitates a more efficient energy transfer and interaction, ultimately leading to an increase in the amplitude of the THG coefficients.

Figure 9 illustrates the THG coefficients at different applied hydrostatic pressure and temperature. In Fig. 9a, the third-harmonic generation (THG) coefficients at different applied hydrostatic pressures are presented. The observations in this figure indicate a slight redshift in the variation of the THG coefficients as the pressure increases. The redshift of the THG coefficients can be attributed to the decrease in the energy difference (E_{10}, E_{20}, E_{30}) between the ground state, first, second, and third excited state as the applied pressure increases. Table 3 also provides information on the product dipole matrix elements ($\mu_{01}\mu_{12}\mu_{23}\mu_{30}$), which show a slight variation with the increment in the applied pressure. However, the magnitude of this variation suggests that the applied pressure has a minimal effect on the dipole matrix elements. In other words, the dipole–dipole interaction between the relevant states, as quantified by the dipole matrix elements, is not significantly influenced by the applied pressure. Considering the negligible change in the dipole matrix elements, the overall effect of increasing pressure on the dipole–dipole interaction, and on the amplitude of the THG coefficients, appears to be insignificant. Therefore, it is expected that the amplitude of the THG resonant peaks will exhibit a small variation with the increment in the applied pressure. In Fig. 9b, the THG coefficients at different applied temperatures are

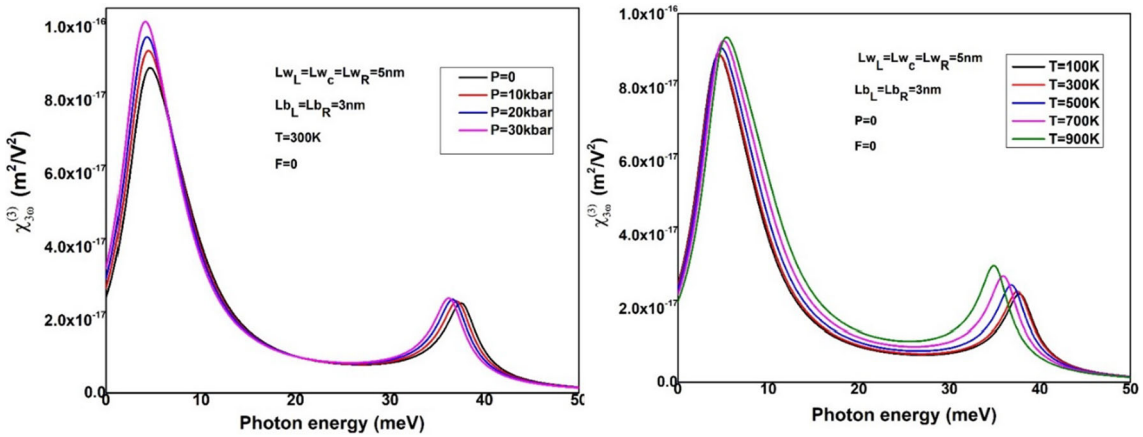

Fig. 9 Variations of THG for different pressures (P) and temperatures (T)

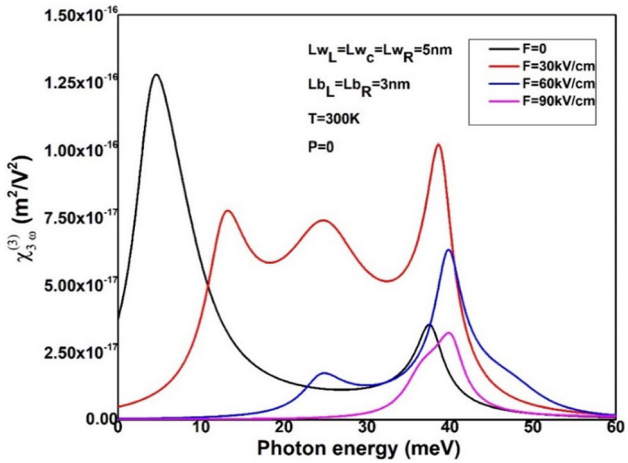

Fig. 10 Variations of THG for the different applied electric fields (F)

shown. The variation of the THG coefficients exhibits a redshift as the temperature increases. This redshift in the THG coefficients can be attributed to the decrease in the energy differences (E_{10}, E_{20}, E_{30}) between the ground, first excited, second excited, and third excited states as the applied temperature increases as seen in Table 4. As the temperature rises, the thermal energy increases, leading to greater thermal broadening of the energy levels. Consequently, the energy differences between the states decrease, resulting in a redshift of the resonant peaks in the THG response. Table 4 also confirms that the product of the products of the dipole matrix elements ($\mu_{01}\mu_{12}\mu_{23}\mu_{30}$) increases with the increase in temperature. The increased temperature causes an elevation in the average kinetic energy of the particles within the system, leading to enhanced electronic transitions. These enhanced transitions influence the dipole matrix elements. The increased dipole matrix elements directly affect the amplitude of the THG coefficients.

In Fig. 10, the effect of an applied electric field on the THG coefficient is shown as a function of the incident photon energy. The main peak of the THG coefficients is located at the resonant peak frequencies, which are determined by the energy difference E_{30}, as indicated in Table 5. Under the applied electric field ($F = 30, 60, 90$ kV/cm), secondary peaks are observed in addition to the main peak. These secondary peaks arise due to the presence of multiple energy differences (E_{10}, E_{20}, E_{30}) that coincide in the system. When the energy differences between the involved states align, a single THG peak appears due to their closeness. In Fig. 10, the peak positions of the THG coefficients shift to higher photon energies as the energy differences between the ground state and third excited state (E_{10}, E_{20}, E_{30}) increase. This shift occurs because the resonance condition for THG is dependent on the energy differences between the states. As these energy differences become larger, the resonant peak frequencies move to higher photon energies. Additionally, the magnitudes of the THG coefficients diminish with an increase in the electric field. This reduction in magnitude is attributed to the decrement in the dipole matrix elements ($\mu_{01}\mu_{12}\mu_{23}\mu_{30}$) under the applied electric field, as indicated in Table 5.

4 Conclusion

The paper describes a numerical investigation of the nonlinear optical coefficients (NOR, SHG, and THG) in an In*P*/InGaAs triple quantum well (TQW) structure under the influence of various external parameters (Lb, Lw, *P*, *T*, *F*). The external fields cause significant changes in the energy levels and wave functions of the system. Resonant peaks are observed in the nonlinear optical properties due to the alignment of energy differences between the involved states. The positions of these peaks can shift to lower or higher photon energies as the energy differences change. Moreover, the magnitudes of the coefficients exhibit variations with changes in the applied parameters. The study reveals that the barrier thickness (Lb) and quantum well width (Lw) result in a redshift in the nonlinear optical properties of the TQW structure. The peak amplitudes of the nonlinear optical coefficients increase with variations in the Lb and Lw parameters. Additionally, applied pressure and temperature can cause redshifts or blueshifts in the nonlinear optical properties, and the amplitude of the resonant peaks can decrease or increase depending on the dipole moment matrix elements. Furthermore, the application of an electric field leads to a shift in the resonant peak positions to higher photon energies. The amplitude of the resonant peaks decreases with the increment in the applied electric fields due to a decrease in the dipole moment matrix elements. In summary, the study demonstrates the ability to manipulate and adjust the optical properties of the TQW structure by applying external fields. These findings have potential applications in the design and optimization of optoelectronic devices based on TQW's potential structure. The parameters explored in this study can be utilized to tune the nonlinear optical properties of the structure and enhance the performance of optoelectronic devices. This investigation contributes to the understanding of the nonlinear optical properties of quantum wells, providing valuable insights for researchers in this field.

Acknowledgements The authors would like to thank the Deanship of Scientific Research at Umm Al-Qura University for supporting this work by Grant Code: (23UQU0000000DSR001).

Data Availability Statement This manuscript has associated data in a data repository. [Authors' comment: The data can be obtained on demand.]

Declarations

Conflict of interest Not applicable.

References

1. A.Y. Cho, J.R. Arthur, Molecular beam epitaxy. Prog. Solid State Chem.. Solid State Chem. **10**, 157–191 (1975)
2. M. Sundaram, S.A. Chalmers, P.F. Hopkins, A.C. Gossard, New quantum structures. Science **254**, 1326–1335 (1991)
3. M.B. Panish, Molecular beam epitaxy. Science **208**, 916–922 (1980)
4. C. Sirtori, F. Capasso, D.L. Sivco, A.Y. Cho, Giant, triply resonant, third-order nonlinear susceptibility $X^{(3)3w}$ in coupled quantum wells. Phys. Rev. Lett. **68**, 1010–1013 (1992)
5. M.C. Onyeaju, J.O.A. Idiodi, A.N. Ikot, M. Solaimani, H. Hassanabadi, Linear and nonlinear optical properties in spherical quantum dots: Manning–Rosen potential. J. Opt. **46**, 254–264 (2017)
6. M.C. Onyeaju, J.O.A. Idiodi, A.N. Ikot, M. Solaimani, H. Hassanabadi, Linear and nonlinear optical properties in spherical quantum dots: generalized hulthén potential. Few-Body Syst. **57**, 793–805 (2016)
7. G. Liu, K. Guo, H. Hassanabadi, L. Lu, Linear and nonlinear optical properties in a disk-shaped quantum dot with a parabolic potential plus a hyperbolic potential in a static magnetic field. Physica B B **407**, 3676–3682 (2012)
8. L. Lu, W. Xie, H. Hassanabadi, Linear and nonlinear optical absorption coefficients and refractive index changes in a two-electron quantum dot. J. Appl. Phys. **109**, 063108 (2011)
9. L. Lu, W. Xie, H. Hassanabadi, The effects of intense laser on nonlinear properties of shallow donor impurities in quantum dots with the Woods–Saxon potential. J. Lumin.Lumin. **131**, 2538–2543 (2011)
10. E. Leobandung, L. Guo, S.Y. Chou, Single hole quantum dot transistors in silicon. Appl. Phys. Lett. **67**, 2338 (1995)
11. K. Imamura, Y. Sugiyama, Y. Nakata, S. Muto, N. Yokoyama, New optical memory structure using self-assembled InAs quantum dots. Jpn. J. Appl. Phys.. J. Appl. Phys. **34**, 1445 (1995)
12. F.D.P. Alves, G. Karunasiri, N. Hanson, M. Byloos, H.C. Liu, A. Bezinger, M. Buchanan, NIR, MWIR and LWIR quantum well infrared photodetector using interband and intersubband transitions. Infrared Phys. Technol. **50**, 182–186 (2007)
13. N. Bouarissa, Piezoelectric and electromechanical coupling constants for $GaxIn_{1-x}Sb$ semiconducting alloys. Philos. Mag. Lett. **99**, 138–145 (2019)
14. B. Li, K.-X. Guo, Z.-L. Liu, Y.-B. Zheng, Nonlinear optical rectification in parabolic quantum dots in the presence of electric and magnetic fields. Phys. Lett. A **372**, 1337–1340 (2008)
15. B.O. Alaydin, Effect of high bandgap AlAs quantum barrier on electronic and optical properties of In070Ga0.30As/Al0.60In0.40As superlattice under applied electric field for laser and detector applications. Int. J. Mod. Phys. B **35**, 2150027 (2021)
16. D. Altun, O. Ozturk, B.O. Alaydin, E. Ozturk, Linear and nonlinear optical properties of a superlattice with periodically increased well width under electric and magnetic fields. Micro Nanostruct. **166**, 207225 (2022)
17. E. Kaynar, B.O. Alaydin, Optical properties of $AlxInyGa_{1-x-y}As/AlzGa_wIn_{1-z-w}As$ quantum wells under electric and magnetic fields for telecommunication applications. Eur. Phys. J. Plus **138**, 121 (2023)
18. D. Makhlouf, M. Choubani, F. Saidi, H. Maaref, Applied electric and magnetic fields effects on the nonlinear optical rectification and the carrier's transition lifetime in InAs/GaAs core/shell quantum dot. Mater. Chem. Phys. **267**, 124660 (2021)
19. N. Zeiri, N. Sfina, S. Abdi-Ben Nasrallah, M. Said, Intersubband resonant enhancement of the nonlinear optical properties in asymmetric (CdS/ZnSe)/X-BeTe based quantum wells. Opt. Mater. **35**, 875–880 (2013)
20. S. Dahiya, S. Lahon, R. Sharma, Effects of temperature and hydrostatic pressure on the optical rectification associated with the excitonic system in a semi-parabolic quantum dot. Physica E E **118**, 113918 (2020)

21. E. Kasapoglu, I. Sökmen, The effects of intense laser field and electric field on intersubband absorption in a double-graded quantum well. Physica B B **403**, 3746–3750 (2008)
22. R. BenMahrsia, M. Choubani, L. Bouzaiene, H. Maaref, Nonlinear optical rectification in a vertically coupled lens-shaped InAs/GaAs quantum dots with wetting layers under hydrostatic pressure and temperature. J. Alloys Compd. **671**, 200–207 (2016)
23. B. Chen, K.-X. Guo, R.-Z. Wang, Z.-H. Zhang, Z.-L. Liu, Linear and nonlinear intersubband optical absorption in double triangular quantum wells. Solid State Commun.Commun. **149**, 310–314 (2009)
24. U. Yesilgul, H. Sari, F. Ungan, J.C. Martínez-Orozco, R.L. Restrepo, M.E. Mora-Ramos, C.A. Duque, I. Sökmen, Effects of electromagnetic fields on the nonlinear optical properties of asymmetric double quantum well under intense laser field. Chem. Phys. **485–486**, 81–87 (2017)
25. S. Sakiroglu, U. Yesilgul, F. Ungan, C.A. Duque, E. Kasapoglu, H. Sari, I. Sokmen, Electronic band structure of GaAs/$Al_xGa_{1-x}As$ superlattice in an intense laser field. J. Lumin.Lumin. **132**, 1584–1588 (2012)
26. F. Ungan, U. Yesilgul, S. Şakiroğlu, E. Kasapoglu, H. Sari, I. Sökmen, Effects of an intense, high-frequency laser field on the intersubband transitions and impurity binding energy in semiconductor quantum wells. Phys. Lett. A **374**, 2980–2984 (2010)
27. N. Eseanu, Simultaneous effects of laser field and hydrostatic pressure on the intersubband transitions in square and parabolic quantum wells. Phys. Lett. A **374**, 1278–1285 (2010)
28. S. Paul, J.B. Roy, P.K. Basu, Empirical expressions for the alloy composition and temperature dependence of the band gap and intrinsic carrier density in $Ga_xIn_{1-x}As$. J. Appl. Phys. **69**, 827–829 (1991)
29. i. InP, InP Band Structure and Carrier Concentration (2023)
30. i. InGaAs, InGaAs Band Structure and Carrier Concentration (2023)
31. B. Soucail, P. Voisin, M. Voos, D. Rondi, J. Nagle, B.D. Cremoux, Optical investigations of the band offsets in an InGaAs-InGaAsP-InP double-step heterostructure. Semiconduct. Sci. Technol. **5**, 918 (1990)
32. P. Başer, S. Elagoz, The hydrostatic pressure and temperature effects on hydrogenic impurity binding energies in lattice matched InP/In0.53Ga0.47As/InP square quantum well. Superlattices Microstruct. Microstruct. **102**, 173–179 (2017)
33. S. Adachi, *Properties of Group eIV, III–V and II–VI Semiconductors* (Willey, 2005)
34. M.E. Mora-Ramos, C.A. Duque, E. Kasapoglu, H. Sari, I. Sökmen, Electron-related nonlinearities in GaAs–Ga1−xAlxAs double quantum wells under the effects of intense laser field and applied electric field. J. Lumin.Lumin. **135**, 301–311 (2013)
35. J.C. Martínez-Orozco, M.E. Mora-Ramos, C.A. Duque, Nonlinear optical rectification and second and third harmonic generation in GaAs δ-FET systems under hydrostatic pressure. J. Lumin.Lumin. **132**, 449–456 (2012)
36. M.E. Mora-Ramos, C.A. Duque, E. Kasapoglu, H. Sari, I. Sökmen, Linear and nonlinear optical properties in a semiconductor quantum well under intense laser radiation: effects of applied electromagnetic fields. J. Lumin.Lumin. **132**, 901–913 (2012)
37. Y.B. Yu, H.J. Wang, Third-harmonic generation in two-dimensional pseudo-dot system with an applied magnetic field. Superlattices Microstruct. Microstruct. **50**, 252–260 (2011)
38. A.S. Durmuslar, M.E. Mora-Ramos, F. Ungan, Nonlinear optical properties of n-type asymmetric double delta doped quantum wells: role of high-frequency laser radiation, doping concentration and well width. Eur. Phys. J. Plus **135**, 442 (2020)
39. R. Khordad, Effect of position-dependent effective mass on linear and nonlinear optical properties of a cubic quantum dot. Physica B B **406**, 3911–3916 (2011)

About this journal

Electronic ISSN
2190-5444

Co-Publisher information
The *European Physical Journal* is jointly published by EDP Sciences, Società Italiana di Fisica and Springer Berlin Heidelberg.

Abstracted and indexed in

ANVUR
Astrophysics Data System (ADS)
BFI List
Baidu
CLOCKSS
CNKI
CNPIEC
Chemical Abstracts Service (CAS)
Current Contents/Physical, Chemical and Earth Sciences
Dimensions
EBSCO Discovery Service
Google Scholar
INIS Atomindex
INSPEC
INSPIRE
Japanese Science and Technology Agency (JST)
Journal Citation Reports/Science Edition
Naver
Norwegian Register for Scientific Journals and Series
OCLC WorldCat Discovery Service
Portico
ProQuest Advanced Technologies & Aerospace Database
ProQuest-ExLibris Primo
ProQuest-ExLibris Summon
SCImago
SCOPUS
Science Citation Index
Science Citation Index Expanded (SCIE)
TD Net Discovery Service
UGC-CARE List (India)
Wanfang

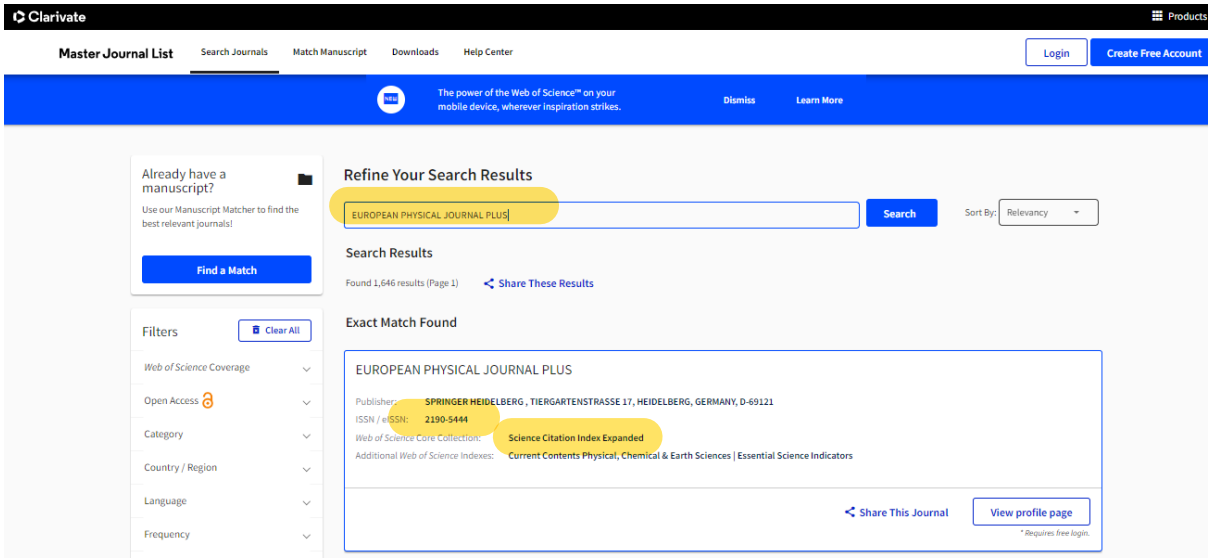

EUROPEAN PHYSICAL JOURNAL PLUS

Publisher name: SPRINGER HEIDELBERG

Journal Impact Factor ™

3.4	3.2
2022	Five Year

JCR Category	Category Rank	Category Quartile
PHYSICS, MULTIDISCIPLINARY *in SCIE edition*	29/85	Q2

Source: Journal Citation Reports 2022. Learn more

Journal Citation Indicator ™ New

0.89	0.94
2022	2021

JCI Category	Category Rank	Category Quartile
PHYSICS, MULTIDISCIPLINARY *in SCIE edition*	27/111	Q1

29